

## Efficient quantum simulation of electron-phonon systems by variational basis state encoder

Weitang Li<sup>1</sup>, Jiajun Ren<sup>2</sup>, Sainan Huai<sup>1</sup>, Tianqi Cai<sup>1</sup>, Zhigang Shuai<sup>3,4,\*</sup> and Shengyu Zhang<sup>1,†</sup><sup>1</sup>Tencent Quantum Lab, Tencent, Shenzhen 518057, China<sup>2</sup>College of Chemistry, Beijing Normal University, Beijing 100875, China<sup>3</sup>Department of Chemistry, Tsinghua University, Beijing 100084, China<sup>4</sup>School of Science and Engineering, The Chinese University of Hong Kong, Shenzhen 518172, China

(Received 11 January 2023; accepted 4 April 2023; published 21 April 2023)

Digital quantum simulation of electron-phonon systems requires truncating infinite phonon levels into  $N$  basis states and then encoding them with qubit computational basis. Unary encoding and binary encoding are the two most representative encoding schemes, which demand  $O(N)$  and  $O(\log N)$  qubits as well as  $O(N)$  and  $O(N \log N)$  quantum gates, respectively. In this paper, we propose a variational basis state encoding algorithm that reduces the scaling of the number of qubits and quantum gates to both  $O(1)$  for systems obeying the area law of entanglement entropy. The cost for the scaling reduction is a constant amount of additional measurement. The accuracy and efficiency of the approach are verified by both numerical simulation and realistic quantum hardware experiments. In particular, we find using one or two qubits for each phonon mode is sufficient to produce quantitatively correct results across weak and strong coupling regimes. Our approach paves the way for practical quantum simulation of electron-phonon systems on both near-term hardware and error-corrected quantum computers.

DOI: [10.1103/PhysRevResearch.5.023046](https://doi.org/10.1103/PhysRevResearch.5.023046)

## I. INTRODUCTION

Electron-phonon couplings are pervasive in quantum materials, governing phenomena such as charge transport in semiconductors [1], vibrational spectra [2], polaron formation [3], and superconductivity [4]. Classically, expensive numerical methods such as density matrix renormalization group (DMRG) and quantum Monte Carlo are required to accurately simulate electron-phonon systems due to the interior many-body interaction [5–11]. Quantum computers hold promise for the simulation of quantum systems with exponential speedup over classical computers [12]. In the wake of the tremendous progress in the implementation of quantum computers [13,14] and the dawning of the noisy intermediate-scale quantum era [15], how to solve electron-phonon coupling problems with quantum computers has attracted a lot of research interest [16–21].

A prominent problem for the digital quantum simulation of electron-phonon systems is how to encode the infinite phonon states with finite quantum computational basis states. The first step is usually truncating the infinite phonon states into  $N$  basis states  $\{|m\rangle\}$  and then the second step is encoding  $\{|m\rangle\}$  into quantum computational basis  $\{|n\rangle\}$ . The phonon basis

states are usually the  $N$  lowest harmonic oscillator eigenstates or  $N$  uniformly distributed grid basis states. There are two established strategies to perform the encoding  $\{|m\rangle\} \mapsto \{|n\rangle\}$  [22,23]. The first is unary encoding [24,25], in which each  $|m\rangle$  is encoded to  $|00\dots 1_m\dots 00\rangle$ , and the total number of qubits required scales as  $O(N)$ . The second is binary encoding, in which each  $|m\rangle$  is encoded to  $\prod_i | \lfloor \frac{m}{2^i} \rfloor \bmod 2 \rangle$  represented by  $O(\log N)$  qubits [16–18]. In terms of two-qubit gates required to simulate quantum operators such as  $\hat{b}^\dagger \pm \hat{b}$  and  $\hat{b}^\dagger \hat{b}$ , unary encoding scales as  $O(N)$  and binary encoding scales as  $O(N \log N)$  [23]. The features of unary encoding and binary encoding are summarized in Table I. Compared to the simulation of electrons, the simulation of phonons consumes quantum resources in a much faster manner, which becomes the bottleneck for efficient quantum simulation of electron-phonon systems.

In this paper, we propose a basis encoding scheme called variational encoding. Variational encoding maps linear combinations of  $|m\rangle$  that are most entangled to the simulated system into the computational basis, i.e.,  $\sum_m C_{mn} |m\rangle \mapsto |n\rangle$ , where  $C_{mn}$  is determined by variational principle. The advantage of our approach is that, by encoding only the most entangled states and discarding the ones with little entanglement, the size of  $\{|n\rangle\}$  can be made irrelevant to the size of  $\{|m\rangle\}$ . In other words, the number of qubits required scales as  $O(1)$ . Consequently, the scaling for the number of gates is also  $O(1)$ . The premise of the scaling reduction is the area law of entanglement entropy. Variational encoding is best suited to work in combination with variational quantum algorithms such as the variational quantum eigensolver (VQE) [26,27] and variational quantum dynamics (VQD) [28,29]. In addition, the variational encoding is also compatible with Trotterized time

\*zgshuai@tsinghua.edu.cn

†shengyuzhang@tencent.com

TABLE I. Comparison of traditional encoding schemes and the proposed variational encoding in terms of encoding formula, the number of qubits  $N_{\text{qubit}}$  required, and the number of quantum gates  $N_{\text{gate}}$  required to simulate common phonon operators such as  $\hat{b}^\dagger \pm \hat{b}$  and  $\hat{b}^\dagger \hat{b}$ .

Scheme	Formula	$N_{\text{qubit}}$	$N_{\text{gate}}$
Unary	$ m\rangle \mapsto  00\dots 1_m\dots 00\rangle$	$O(N)$	$O(N)$
Binary	$ m\rangle \mapsto \prod_i  \lfloor \frac{m}{2^i} \rfloor \bmod 2\rangle$	$O(\log N)$	$O(N \log N)$
Variational	$\sum_m C_{mn}  m\rangle \mapsto  n\rangle$	$O(1)$	$O(1)$

evolution and quantum phase estimation (QPE) [12,30,31]. Numerical simulation and experiments on realistic quantum hardware based on the Holstein model and spin-boson model shows that using one or two qubits for each phonon mode is typically sufficient for highly accurate results, even in the strong coupling regime.

## II. VARIATIONAL BASIS STATE ENCODER

In this section, we present a more rigorous formulation of the variational basis state encoder. To encode each phonon mode  $l$ , encoded by  $N_l$  qubits, we define the variational basis state encoder  $\hat{B}[l]$  as follows:

$$\hat{B}[l] := \sum_m \sum_{n=1}^{2^{N_l}} C[l]_{mn} |n\rangle_l |m\rangle, \quad (1)$$

with orthonormal constraint

$$\hat{B}[l]\hat{B}[l]^\dagger = \hat{I} \quad (2)$$

or, equivalently,

$$\sum_m C[l]_{mn} C[l]_{m'n'}^* = \delta_{nn'}. \quad (3)$$

In this paper, we use  $|m\rangle$  to represent phonon states and  $|n\rangle$  to represent qubit states. Equation (1) can be rewritten as

$$\hat{B}[l] = \sum_{n=1}^{2^{N_l}} |n\rangle_l \sum_m C[l]_{mn} |m\rangle, \quad (4)$$

and it is clear that  $\hat{B}$  performs  $\sum_m C_{mn} |m\rangle \mapsto |n\rangle$ . The original Hamiltonian in  $|m\rangle$  basis  $\hat{H}$  can then be encoded to  $|n\rangle$  basis using the following expression:

$$\hat{H} := \prod_l \hat{B}[l] \hat{H} \prod_l \hat{B}[l]^\dagger. \quad (5)$$

For both static and dynamic cases, encoder coefficients  $C$  are determined by variational principle. In the remainder of the section, we will derive the equation for  $C$ . We use atomic units throughout the paper.

### A. Time-independent equation

Suppose the quantum circuit is parameterized by  $|\phi\rangle = \prod_k e^{i\theta_k \hat{R}_k} |\phi_0\rangle$ , and then the ground state Lagrangian with

multipliers  $\lambda_{lmn'}$  is

$$\mathcal{L} = \langle \phi | \hat{H} | \phi \rangle + \sum_{lmn'} \lambda_{lmn'} \left( \sum_m C[l]_{mn} C[l]_{mn'}^* - \delta_{nn'} \right). \quad (6)$$

Taking the derivative with respect to  $\theta_k$  immediately leads to traditional VQE with encoded Hamiltonian  $\hat{H}'$ :

$$\frac{\partial \langle \phi | \hat{H} | \phi \rangle}{\partial \theta_k} = 0. \quad (7)$$

Taking the derivative with respect to  $C[l]_{mn}$  and setting it to 0 yields

$$\langle \phi | n \rangle_l \langle m | \hat{H}'[l] | \phi \rangle + \sum_{n'} \lambda_{lmn'} C[l]_{mn'}^* = 0, \quad (8)$$

where  $\hat{H}'[l]$  is the the half-encoded Hamiltonian:

$$\hat{H}'[l] := \prod_{k \neq l} \hat{B}[k] \hat{H} \prod_k \hat{B}[k]^\dagger. \quad (9)$$

Multiply Eq. (8) with  $C[l]_{mn'}$  and use the  $C[l]$  orthonormal condition Eq. (3) to get  $\lambda$ :

$$\lambda_{lmn'} = - \sum_m C[l]_{mn'} \langle \phi | n \rangle_l \langle m | \hat{H}'[l] | \phi \rangle. \quad (10)$$

Define projector

$$\hat{P} := \hat{B}[l]^\dagger \hat{B}[l] = \sum_{mm'} \sum_n |m\rangle_l C[l]_{mn}^* C[l]_{m'n} \langle m'|. \quad (11)$$

Substituting  $\lambda$  [Eq. (10)] into Eq. (8) then yields

$$\langle \phi | n \rangle_l \langle m | \hat{H}'[l] | \phi \rangle - \langle \phi | n \rangle_l \langle m | \hat{P} \hat{H}'[l] | \phi \rangle = 0. \quad (12)$$

Rearranging and rewriting in matrix form, we get the equation for  $C[l]$ :

$$(1 - \hat{P}[l]) \langle \phi | \hat{H}'[l] | \phi \rangle = 0. \quad (13)$$

Here  $C[l]$  is contained in  $\hat{P}[l]$  and  $\hat{H}'[l]$ .

To summarize, circuit parameters  $\theta_k$  are solved by VQE according to Eq. (7), and variational parameters  $C[l]$  are determined by solving Eq. (13) classically. Because Eq. (7) contains  $C[l]$  and Eq. (13) contains  $\theta_k$ ,  $\theta_k$  and  $C[l]$  are solved iteratively until convergence. In the following, this iteration is termed macroiteration to avoid confusion with VQE iteration.

### B. Quantum circuit measurement

In this section, we discuss the quantum circuit measurement required to solve  $C[l]$  from Eq. (13). The key quantity to be computed is matrix  $G[l]_{mn}$ , defined as

$$G[l]_{mn} := \langle \phi | n \rangle_l \langle m | \hat{H}'[l] | \phi \rangle. \quad (14)$$

Suppose the Hamiltonian can be written as a sum of direct products

$$\hat{H} = \sum_x^M \hat{h}_x, \quad \hat{h}_x = \prod_k \hat{h}[k]_x, \quad (15)$$

where  $M$  is the total number of terms in the Hamiltonian and  $\hat{h}[k]_x$  acts on the  $k$ th degree of freedom. Similar to the encoded

Hamiltonian, the encoded local operator is denoted as  $\hat{h}[k]_x$ :

$$\hat{h}[k]_x := \hat{B}[k]\hat{h}[k]_x\hat{B}[k]^\dagger. \quad (16)$$

For electron degrees of freedom, a dummy encoder  $\hat{B}[k] = \hat{I}$  is used for notational simplicity.  $G[I]_{mn}$  can then be written as

$$G[I]_{mn} = \sum_x^M \langle \phi | n \rangle_{l \ l} \langle m | \hat{h}[I]_x \hat{B}[I]^\dagger \prod_{k \neq l} \hat{h}[k]_x | \phi \rangle. \quad (17)$$

Next, represent  $\hat{h}[I]_x$  in operator form:

$$\hat{h}[I]_x = \sum_{mm'} h[I]_{xmn} | m' \rangle_{l \ l} \langle m |. \quad (18)$$

$G[I]_{mn}$  then becomes

$$G[I]_{mn} = \sum_x^M \sum_{m'n'} h[I]_{xmn} C[I]_{m'n'} J[I]_{xmn'}, \quad (19)$$

$$J[I]_{xmn'} := \langle \phi | n \rangle_{l \ l} \langle n' | \prod_{k \neq l} \hat{h}[k]_x | \phi \rangle.$$

Thus, to evaluate  $G[I]_{mn}$  it is sufficient to measure  $J[I]_{xmn'}$ .  $|n\rangle_{l \ l} \langle n'|$ , in general, is not Hermitian, but the real and imaginary parts can be measured separately with  $(|n\rangle_{l \ l} \langle n'| + |n'\rangle_{l \ l} \langle n|)$  and  $i(|n'\rangle_{l \ l} \langle n| - |n\rangle_{l \ l} \langle n'|)$ .

Assuming the number of measurement shots for each Pauli string is  $N_{\text{shots}}$ , the number of measurements to determine  $J[I]$  is thus  $O(2^{N_l} M N_{\text{shots}})$ , which is polynomial to the system size and does not increase with  $N$ . After  $J[I]$  is measured, evaluating  $G[J]$  and the left-hand side of Eq. (13) scales as  $O(2^{N_l} N^2 M)$  by matrix multiplication on a classical computer. Considering the measurement of a parameterized quantum circuit takes a much longer time than a float-point number operation on classical computers, the classical workload is negligible compared to the additional measurements for reasonable values of  $N_{\text{shots}}$  and  $N$ , such as  $N_{\text{shots}} = 4096$  and  $N = 64$ . Thus the reduction in quantum resources is not achieved by increasing classical resources [32]. If the number of phonon modes is assumed to be linear with  $M$  and each  $C[I]$  is updated independently, then the total number of measurements for all  $C[I]$  is  $O(2^{N_l} M^2 N_{\text{shots}})$ . The measurement overhead increases exponentially with  $N_l$ . Due to arguments presented later,  $N_l$  is usually small and does not increase with system size. From numerical experiments, we find  $N_l \leq 2$  is sufficient to produce excellent results.

### C. Time-dependent equation

For time-dependent problems, it is convenient to define

$$|\psi\rangle := \prod_l \hat{B}[I]^\dagger | \phi \rangle \quad (20)$$

and use  $\Theta_K$  denote both  $\theta_k$  and  $C[I]$ . The Lagrangian with multipliers  $\lambda_{lmm'}$  and  $\gamma_{lmm'}$  is then

$$\mathcal{L} = \left| i \sum_K \frac{\partial |\psi\rangle}{\partial \Theta_K} \dot{\Theta}_K - \hat{H} |\psi\rangle \right|^2 + \sum_{lmm'} \lambda_{lmm'} \Re \sum_m C[I]_{mn}^* \dot{C}[I]_{mn} + \sum_{lmm'} \gamma_{lmm'} \Im \sum_m C[I]_{mn}^* \dot{C}[I]_{mm'}. \quad (21)$$

The constraints ensure that  $C[I]_{mn}$  remains orthonormal during time evolution. Taking the derivative with respect to  $\Theta_K$  yields

$$\begin{aligned} \frac{\partial \mathcal{L}}{\partial \Theta_K} &= \sum_J \frac{\partial \langle \psi | \partial |\psi\rangle}{\partial \Theta_J} \frac{\partial |\psi\rangle}{\partial \Theta_K} \dot{\Theta}_J + \sum_J \frac{\partial \langle \psi | \partial |\psi\rangle}{\partial \Theta_K} \frac{\partial |\psi\rangle}{\partial \Theta_J} \dot{\Theta}_J \\ &+ i \frac{\partial \langle \psi | \partial |\psi\rangle}{\partial \Theta_K} \hat{H} |\psi\rangle - i \langle \psi | \hat{H} \frac{\partial |\psi\rangle}{\partial \Theta_K} \\ &+ \sum_{lmm'} \lambda_{lmm'} \Re \sum_m C[I]_{mn}^* \frac{\partial \dot{C}[I]_{mn}}{\partial \dot{\Theta}_K} \\ &+ \sum_{lmm'} \gamma_{lmm'} \Im \sum_m C[I]_{mn}^* \frac{\partial \dot{C}[I]_{mm'}}{\partial \dot{\Theta}_K}. \end{aligned} \quad (22)$$

The subsequent derivation involves a more intricate process similar to that of Eq. (13). Elaborate details are documented in Appendix A. Here, we provide an outline of the crucial steps. First, consider the case where  $\Theta_K = \theta_k$  and we find that the equation of motion for  $\theta_k$  is the same as vanilla VQD with encoded Hamiltonian  $\hat{H}$ :

$$\sum_j \Re \frac{\partial \langle \phi | \partial |\phi\rangle}{\partial \theta_k} \frac{\partial |\phi\rangle}{\partial \theta_j} \dot{\theta}_j = \Im \frac{\partial \langle \phi | \partial |\phi\rangle}{\partial \theta_k} \hat{H} |\phi\rangle. \quad (23)$$

Next, consider the case where  $\Theta_K = C[I]$ , which ultimately leads to the following equation for  $\dot{C}[I]$ :

$$i \rho[I] \dot{C}[I]^* = (1 - \hat{P}[I]) \langle \phi | \hat{H}'[I] | \phi \rangle, \quad (24)$$

where  $\rho[I]_{mm'} = \text{Tr}\{\langle \phi | n \rangle_{l \ l} \langle n' | \phi \rangle\}$  is the reduced density matrix for the  $N_l$  qubits of  $|\phi\rangle$ . Equation (13) represents a  $\dot{C}[I] = 0$  stationary point during real and imaginary time evolution. The measurement cost is the same as the ground state algorithm.

While we have relied on parameterized quantum circuits for our derivation thus far, it is worth noting that incorporating the variational encoder into Trotterized time evolution and QPE is a straightforward extension. The VQD step described by Eq. (23) can be naturally replaced by a Suzuki-Trotter time evolution step  $e^{-i\hat{H}\tau} \approx \prod_x^M e^{-i\hat{h}_x\tau}$  on a digital quantum simulator, so that Hamiltonian simulation is performed via Trotterized time evolution instead of VQD. To update  $C[I]$  based on Eq. (24), measurements on the circuit should be performed for every or every several Trotter steps. The variationally encoded ground state can then be prepared by adiabatic state preparation, whose energy is accessible by QPE using  $\hat{H}$ .

### D. Variational basis state encoder as an ansatz

It is instructive to observe that if the variational basis encoder is viewed as a wave function ansatz  $|\psi\rangle$ , then the algorithm proposed in this paper can be viewed as a generalization for the local basis optimization method for DMRG [33,34] or a special case of the recently proposed quantum-classical hybrid tensor network [35]. Thus,  $\hat{B}[I]$  captures the  $2^{N_l}$  phonon states that are most entangled with the rest of the system. For local Hamiltonians obeying the area law, the entanglement entropy between one phonon mode and the rest of the system  $S$  is a constant [36]. Consequently,  $|\langle \psi | \Psi \rangle|^2$ , the fidelity between the approximated encoded state

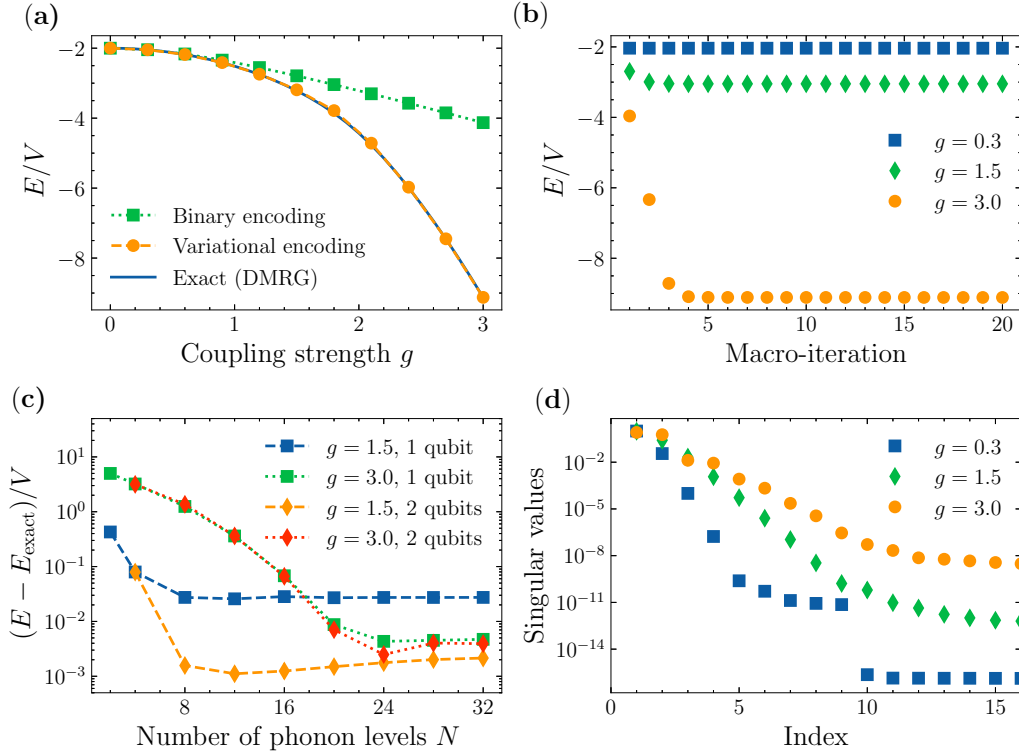


FIG. 1. Numerical simulation results for the ground state of the Holstein model. (a) Ground state energy by binary encoding and variational encoding with different coupling strength  $g$ ; (b) Convergence of ground state energy with respect to the macroiteration for variational encoding. (c) Ground state energy error for the variational encoding method at different numbers of phonon basis states  $N$ . (d) The singular values for the Schmidt decomposition between the last phonon mode and the rest of the system.

and the target state has a lower bound of  $\frac{2^{N_l}}{e^g}$ , which lays the theoretical foundation for the effectiveness of the variational encoding approach to ground-state and low-lying excited state problems.

### III. SIMULATIONS

#### A. Numerical simulation on a noiseless simulator

The variational basis state encoder is first tested for VQE simulation of the one-dimensional Holstein model [37,38],

$$\hat{H} = - \sum_{\langle i,j \rangle} V \hat{a}_i^\dagger \hat{a}_j + \sum_i \omega \hat{b}_i^\dagger \hat{b}_i + \sum_i g \omega \hat{a}_i^\dagger \hat{a}_i (\hat{b}_i^\dagger + \hat{b}_i), \quad (25)$$

where  $\hat{a}$  and  $\hat{b}$  are annihilation operators for electron and phonon, respectively,  $V$  is the hopping coefficient,  $\langle i, j \rangle$  denotes nearest-neighbor pairs with periodic boundary conditions,  $\omega$  is the vibration frequency, and  $g$  is dimensionless coupling constant. In the following, we assume  $V = \omega = 1$  and adjust  $g$  for different coupling strengths. We consider a three-site system corresponding to  $3(N_l + 1)$  qubits. We use binary encoding to represent traditional encoding approaches. Unary encoding is expected to produce similar results with binary encoding only with different quantum resource budgets. We devise the following ansatz:

$$|\phi\rangle = \prod_l \left\{ \prod_{(j,k)} e^{\theta_{ljk} (\hat{a}_j^\dagger \hat{a}_k - \hat{a}_k^\dagger \hat{a}_j)} \prod_j e^{\theta_{l,j} \hat{a}_j^\dagger \hat{a}_j (\hat{b}_j^\dagger - \hat{b}_j)} \right\} |\phi_0\rangle, \quad (26)$$

where  $L$  is the number of layers and  $L = 3$  is adopted. More details of the simulation are included in Appendix B.

We first compare the accuracy of the variational encoding and the binary encoding with  $N_l = 1$ . It is clear from Fig. 1(a) that variational encoding is significantly more accurate than binary encoding, especially at the strong coupling regime. Within the setup, binary encoding uses only two phonon basis states to describe each phonon mode, yet the variational encoding is allowed to use up to 32 phonon basis states before combining them into the most entangled states. We note that the quantum circuit used for variational encoding and binary encoding is essentially the same. The number of macroiterations to determine  $C[l]$  is found to be rather small, as shown in Fig. 1(b). Fully converged results are obtained within five iterations. In Fig. 1(c), we show more details of the error for the variational approach. The simulation error typically decreases exponentially with respect to the number of phonon levels  $N$  included in  $C[l]$ . It is worth noting that quantum computational resources, including the number of qubits, the number of gates in the circuit, and the number of measurements remain constant when  $N$  is increased from 2 to 32. Furthermore, by using two qubits to encode each mode, it is possible to further reduce the error at the  $N \rightarrow \infty$  limit. When  $g = 3.0$ , the error is not sensitive to  $N_l$ , which implies that the error is dominated by other sources such as limitations of the ansatz, instead of the small  $N_l$ . Figure 1(d) shows the singular values for the Schmidt decomposition between the last phonon mode and the rest of the system by DMRG. The exponential decay ensures the fast convergence

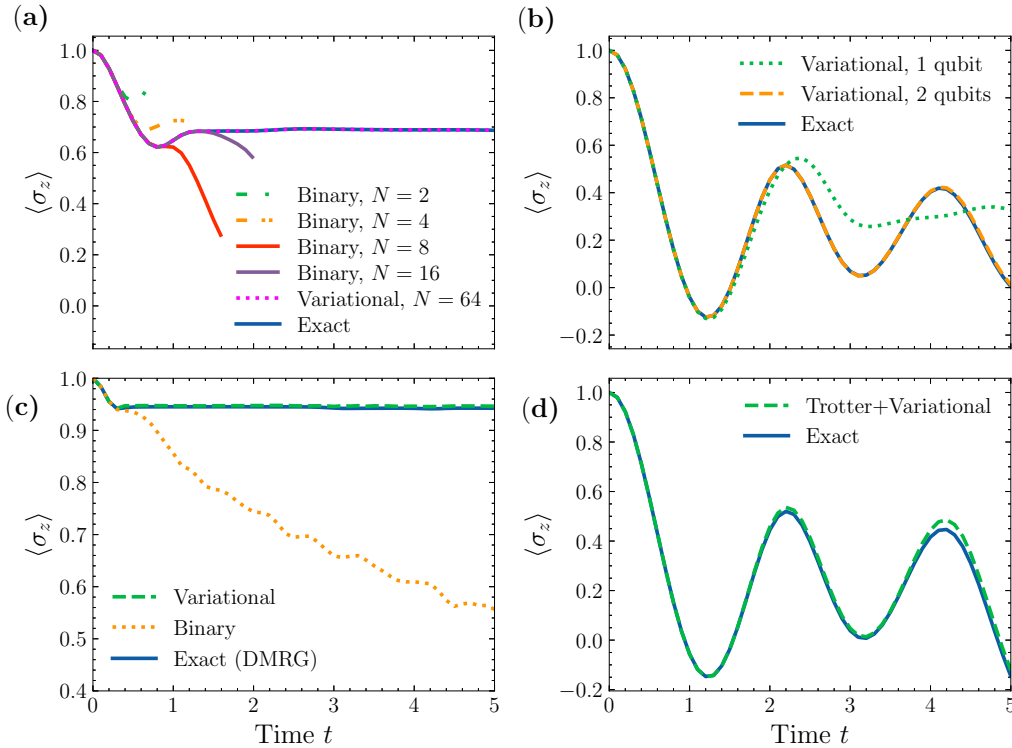


FIG. 2. Numerical simulation results for the spin-relaxation dynamics of the spin-boson model. (a) Comparison between binary encoding with different numbers of phonon basis states and variational encoding for a one-mode spin-boson model. (b) Variational encoding with different numbers of encoding qubits  $N_l$  for a two-mode spin-boson model. (c) Comparison between binary encoding and variational encoding for an eight-mode spin-boson model with sub-Ohmic spectral density. (d) Trotterized time evolution with variational encoding based on a one-mode spin-boson model.

of  $N_l$ . The von Neumann entropy  $S$  for the three systems is found to be 0.01, 0.25, and 0.65, respectively. We also note the  $g = 1.5$  case has the largest third singular value, which explains why setting  $N_l = 2$  significantly reduces the  $g = 1.5$  error in Fig. 1(c).

We now turn to the spin-relaxation dynamics of the spin-boson model [39], described by the Hamiltonian

$$\hat{H} = \frac{\epsilon}{2} \hat{\sigma}_z + \Delta \hat{\sigma}_x + \sum_j g_j \omega_j \hat{\sigma}_z (\hat{b}_j^\dagger + \hat{b}_j) + \sum_j \omega_j \hat{b}_j^\dagger \hat{b}_j, \quad (27)$$

where  $\epsilon$  is the eigenfrequency and  $\Delta$  is the tunneling rate. The coupling term has a similar form with Eq. (25) and is more commonly written as  $\sum_j c_j \hat{\sigma}_z \hat{x}_j$ . For systems in the condensed phase, the coupling is usually characterized by the spectral density function  $\mathcal{J}(\omega) = \frac{\pi}{2} \sum_j \frac{c_j^2}{\omega_j} \delta(\omega - \omega_j)$ . In the following, we assume  $\epsilon = 0$  and  $\Delta = 1$ . We first use VQD for the simulation and discuss Trotterized time evolution at last. The variational Hamiltonian ansatz [40] with three layers is used if not otherwise specified.

The performance of variational encoding and binary encoding is first compared based on a one-mode spin-boson model at the strong coupling ( $\omega = 1$  and  $g = 3$ ) regime, shown in Fig. 2(a). Variational encoding with  $N_l = 1$  generates much more accurate dynamics than binary encoding with fewer qubits and quantum gates. The simulation of binary encoding with  $N_l > 4$  is prohibited by the deep circuit

depth in the ansatz. The variational encoding scheme is exceptionally efficient for this one-mode model because Schmidt decomposition guarantees that two variational bases for the phonon mode are sufficient to exactly represent the system. In Fig. 2(b), a two-mode model with  $\omega_j = \frac{1}{2}, 1$  and  $g_j = \frac{1}{2}, 1$  is used. Variational encoding with  $N_l = 1$  is accurate at  $t < 2$  but as the entanglement builds up the dynamics deviate from the exact solution. Increasing  $N_l$  to two effectively eliminates the error. Next, we move on to a more challenging model with eight modes, in which  $\omega$  and  $g$  are determined by discretizing a sub-Ohmic spectral density  $\mathcal{J}(\omega) = \frac{\pi}{2} \alpha \omega^s \omega_c^{1-s} e^{-\omega/\omega_c}$  following the prescription in the literature [41]. The parameters are  $s = \frac{1}{4}$ ,  $\omega_c = 4$  and  $\alpha = 10$ . As illustrated in Fig. 2(c), variational encoding with  $N_l = 1$  captures the localization behavior yet binary encoding with  $N_l = 1$  completely fails. The number of layers in the variational Hamiltonian ansatz is 8 and 32 for variational and binary encoding, respectively. Figure 2(d) demonstrates the possibility to incorporate the variational basis state encoder into Trotterized time evolution with  $\omega = g = 1$  and  $N_l = 1$ . The measurement and the evolution of  $C[l]$  are performed at each Trotter step.

## B. Verification on a superconducting quantum processor

In this section, we verify the accuracy and efficiency of the variational encoder approach on a superconducting quantum processor [42,43]. We consider the ground state problem of a two-site Holstein model described by Eq. (25) with  $g = 3$

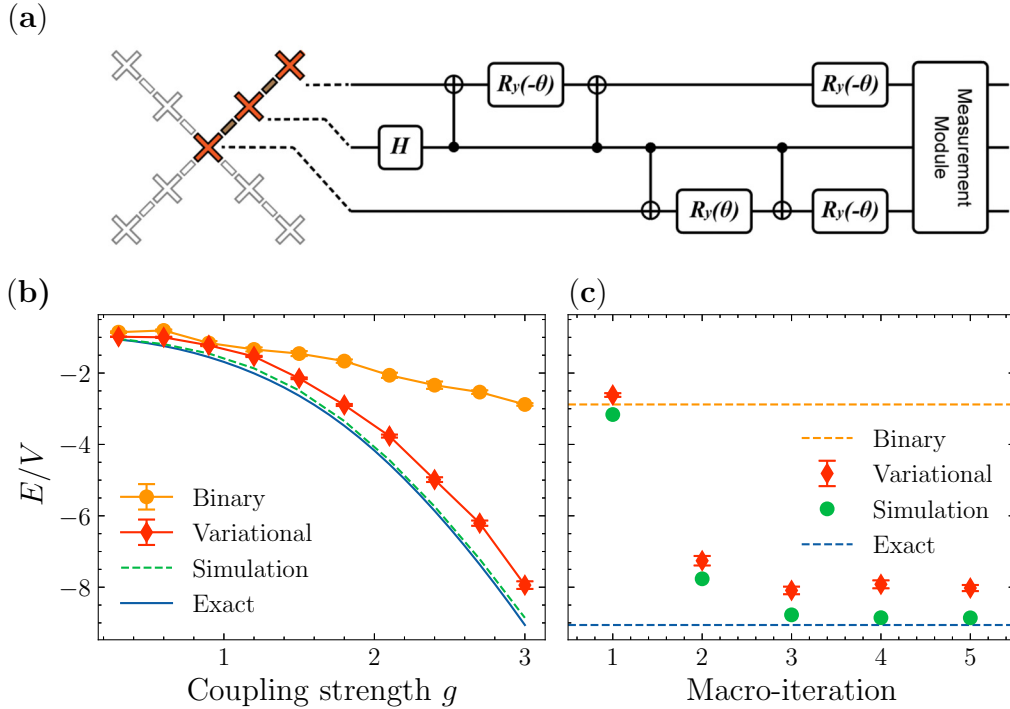


FIG. 3. Quantum hardware experiments for the ground state energy of the Holstein model with variational basis state encoder. (a) Three qubits out of nine qubits of a superconducting quantum processor and a one-parameter circuit are used for the simulation. (b) Ground state energy by binary encoding and variational encoding. (c) Convergence of ground state energy with respect to the macro-iteration for variational encoding.

and  $N_l = 1$ . The two electronic sites are represented by one qubit and the total number of qubits for the system is thus three. The quantum circuit for the simulation is depicted in Fig. 3(a). The electronic degree of freedom is mapped to the second qubit, and the two phonon modes are mapped to the first and the third qubits respectively. There is one parameter to be determined by VQE in the circuit and the same ansatz is used for both binary encoding and variational encoding. More simulation details can be found in the Supplemental Material. In Fig. 3(b), we show the ground state energy by variational encoding from weak to strong coupling, in analog to Fig. 1(a). The simulator result is based on the parameterized quantum circuit described in Fig. 3(a) without considering gate noise and measurement uncertainty. The results in Fig. 3(b) are consistent with those in Fig. 1(a). The residual error is dominated by the intrinsic gate noise in the quantum computer. In Fig. 3(c), we show the convergence with respect to the macro-iteration for variational encoding. The algorithm is resilient to the presence of quantum noise and measurement uncertainty. The convergent energy is reached within five iterations.

#### IV. CONCLUSION

We proposed a variational basis state encoder to encode phonon basis states into quantum computational states for efficient quantum simulation of electron-phonon systems. The proposed variational encoding approach requires only  $O(1)$  qubits and  $O(1)$  quantum gates for systems obeying the area law of entanglement entropy, which is significantly better than

traditional encoding schemes and enables quantum simulation of electron-phonon systems with smaller quantum processors and shallower circuits. The additional measurement required to implement the approach is found to be also  $O(1)$  with respect to the number of phonon basis states and it scales quadratically with the number of Pauli strings in the Hamiltonian. The accuracy of the approach is ensured by the finite entanglement entropy between one phonon mode and the rest of the system in common electron-phonon systems. The variational basis state encoder most naturally works with variational quantum algorithms and is compatible with Trotterized time evolution, adiabatic state preparation, and QPE. Numerical simulation and quantum hardware experiments based on VQE of the Holstein model and dynamics of the spin-boson model indicate that variational encoding is more accurate and resource-efficient than traditional encoding methods. In particular, using one or two qubits to represent each phonon mode is sufficient for accurate simulation even at the strong coupling regime where  $N = 32$  phonon basis states are involved. The approach could also be extended to other quantum simulation problems involving an infinite or large local Hilbert space.

#### ACKNOWLEDGMENTS

We thank Jinzhao Sun and Shixin Zhang for helpful discussions. This work is supported by the National Natural Science Foundation of China through Grants No. 22273005 and No. 21788102. This work is also supported by Shenzhen Science and Technology Program.

### APPENDIX A: DERIVATION OF TIME-DEPENDENT EQUATION

In this Appendix, we derive the time-dependent equation for  $C[l]$ . For time-dependent problems,  $C[l]$ , in general, is complex,

$$C[l] = D[l] - iE[l], \quad (\text{A1})$$

where both  $D[l]$  and  $E[l]$  are real. The minus sign is for convenience, expressing  $\hat{B}^\dagger |\phi\rangle$ . From the definition, we have

$$\frac{\partial |\psi\rangle}{\partial E[l]_{mn}} = i \frac{\partial |\psi\rangle}{\partial D[l]_{mn}}. \quad (\text{A2})$$

The starting point is Eq. (22). We first consider the case of  $\Theta_K = \theta_k$ , and then

$$\begin{aligned} \frac{\partial \mathcal{L}}{\partial \theta_k} &= \sum_J \frac{\partial \langle \psi | \partial |\psi \rangle}{\partial \Theta_J} \frac{\partial |\psi \rangle}{\partial \theta_k} \dot{\Theta}_J + \sum_J \frac{\partial \langle \psi | \partial |\psi \rangle}{\partial \theta_k} \frac{\partial |\psi \rangle}{\partial \Theta_J} \dot{\Theta}_J + i \frac{\partial \langle \psi | \hat{H} |\psi \rangle}{\partial \theta_k} - i \langle \psi | \hat{H} \frac{\partial |\psi \rangle}{\partial \theta_k} \\ &= 2 \sum_J \Re \frac{\partial \langle \psi | \partial |\psi \rangle}{\partial \theta_k} \frac{\partial |\psi \rangle}{\partial \Theta_J} \dot{\Theta}_J - 2 \Im \frac{\partial \langle \psi | \hat{H} |\psi \rangle}{\partial \theta_k}, \end{aligned} \quad (\text{A3})$$

which means at the  $\frac{\partial \mathcal{L}}{\partial \theta_k} = 0$  minimum, we have

$$\sum_J \Re \frac{\partial \langle \psi | \partial |\psi \rangle}{\partial \theta_k} \frac{\partial |\psi \rangle}{\partial \Theta_J} \dot{\Theta}_J = \Im \frac{\partial \langle \psi | \hat{H} |\psi \rangle}{\partial \theta_k}. \quad (\text{A4})$$

Substitute  $\Theta_J$  with  $\theta_k$ ,  $D[l]_{mn}$ , and  $E[l]_{mn}$ :

$$\sum_J \Re \frac{\partial \langle \psi | \partial |\psi \rangle}{\partial \theta_k} \frac{\partial |\psi \rangle}{\partial \Theta_J} \dot{\Theta}_J = \sum_j \Re \frac{\partial \langle \psi | \partial |\psi \rangle}{\partial \theta_k} \frac{\partial |\psi \rangle}{\partial \theta_j} \dot{\theta}_j + \sum_{lmn} \Re \frac{\partial \langle \psi | \partial |\psi \rangle}{\partial \theta_k} \frac{\partial |\psi \rangle}{\partial D[l]_{mn}} \dot{D}[l]_{mn} + \sum_{lmn} \Re \frac{\partial \langle \psi | \partial |\psi \rangle}{\partial \theta_k} \frac{\partial |\psi \rangle}{\partial E[l]_{mn}} \dot{E}[l]_{mn}. \quad (\text{A5})$$

Using Eq. (A2), the last two terms become

$$\sum_{lmn} \Re \frac{\partial \langle \psi | \partial |\psi \rangle}{\partial \theta_k} \frac{\partial |\psi \rangle}{\partial D[l]_{mn}} \dot{D}[l]_{mn} + \sum_{lmn} \Re \frac{\partial \langle \psi | \partial |\psi \rangle}{\partial \theta_k} \frac{\partial |\psi \rangle}{\partial E[l]_{mn}} \dot{E}[l]_{mn} = \sum_{lmn} \Re \frac{\partial \langle \psi | \partial |\psi \rangle}{\partial \theta_k} \frac{\partial |\psi \rangle}{\partial D[l]_{mn}} \dot{C}[l]_{mn}^*, \quad (\text{A6})$$

which is zero because

$$\sum_{mn} \frac{\partial \langle \psi | \partial |\psi \rangle}{\partial \theta_k} \frac{\partial |\psi \rangle}{\partial D[l]_{mn}} \dot{C}[l]_{mn}^* = \sum_{mn} \frac{\partial \langle \phi | \hat{B}[l] |m\rangle_l}{\partial \theta_k} \langle n | \dot{C}[l]_{mn}^* | \phi \rangle = 0, \quad (\text{A7})$$

where the constraint  $\sum_m C[l]_{mn} \dot{C}[l]_{mn}^* = 0$  is used. Thus, the simplified equation of motion reads

$$\sum_j \Re \frac{\partial \langle \psi | \partial |\psi \rangle}{\partial \theta_k} \frac{\partial |\psi \rangle}{\partial \theta_j} \dot{\theta}_j = \Im \frac{\partial \langle \psi | \hat{H} |\psi \rangle}{\partial \theta_k} \quad (\text{A8})$$

or, equivalently,

$$\sum_j \Re \frac{\partial \langle \phi | \partial |\phi \rangle}{\partial \theta_k} \frac{\partial |\phi \rangle}{\partial \theta_j} \dot{\theta}_j = \Im \frac{\partial \langle \phi | \hat{H} |\phi \rangle}{\partial \theta_k}. \quad (\text{A9})$$

In short, the equation of motion for  $\theta_k$  is the same as vanilla VQD with encoded Hamiltonian  $\hat{H}$ .

Next we consider the case of  $\Theta_K = D[l]$  and  $\Theta_K = E[l]$ . After some complex algebra, we have

$$i \sum_J \frac{\partial \langle \psi | \partial |\psi \rangle}{\partial D[l]_{mn}} \frac{\partial |\psi \rangle}{\partial \Theta_J} \dot{\Theta}_J + i \frac{1}{2} \sum_{n'} \lambda_{ln'n} C[l]_{mn'}^* - \frac{1}{2} \sum_{n'} \gamma_{ln'n} C[l]_{mn'}^* = \frac{\partial \langle \psi | \hat{H} |\psi \rangle}{\partial D[l]_{mn}}. \quad (\text{A10})$$

Similar to the case of  $\Theta_K = \theta_k$ , substituting  $\Theta_J$  with  $\theta_k$ ,  $D[l]_{mn}$  and  $E[l]_{mn}$ :

$$\begin{aligned} \sum_J \frac{\partial \langle \psi | \partial |\psi \rangle}{\partial D[l]_{mn}} \frac{\partial |\psi \rangle}{\partial \Theta_J} \dot{\Theta}_J &= \sum_k \frac{\partial \langle \psi | \partial |\psi \rangle}{\partial D[l]_{mn}} \frac{\partial |\psi \rangle}{\partial \theta_k} \dot{\theta}_k + \sum_{km'n'} \frac{\partial \langle \psi | \partial |\psi \rangle}{\partial D[l]_{mn}} \frac{\partial |\psi \rangle}{\partial D[k]_{m'n'}} \dot{C}[k]_{m'n'}^* \\ &= \sum_k \frac{\partial \langle \psi | \partial |\psi \rangle}{\partial D[l]_{mn}} \frac{\partial |\psi \rangle}{\partial \theta_k} \dot{\theta}_k + \sum_{n'} \frac{\partial \langle \psi | \partial |\psi \rangle}{\partial D[l]_{mn}} \frac{\partial |\psi \rangle}{\partial D[l]_{mn'}} \dot{C}[l]_{mn'}^*. \end{aligned} \quad (\text{A11})$$

Here the orthonormal condition is again used. Substitute the equation back into Eq. (A10):

$$i \sum_k \frac{\partial \langle \psi | \partial |\psi \rangle}{\partial D[l]_{mn}} \frac{\partial |\psi \rangle}{\partial \theta_k} \dot{\theta}_k + i \sum_{n'} \frac{\partial \langle \psi | \partial |\psi \rangle}{\partial D[l]_{mn}} \frac{\partial |\psi \rangle}{\partial D[l]_{mn'}} \dot{C}[l]_{mn'}^* + \frac{1}{2} \sum_{n'} (i\lambda_{ln'n} - \gamma_{ln'n}) C[l]_{mn'}^* = \frac{\partial \langle \psi | \hat{H} |\psi \rangle}{\partial D[l]_{mn}}. \quad (\text{A12})$$

Following the same strategy with the derivation of the time-independent equation, multiply Eq. (A12) with  $C[l]_{mn}$ ,

$$i \sum_k \langle \phi | n \rangle_l \langle n' | \frac{\partial |\phi\rangle}{\partial \theta_k} \dot{\theta}_k + \frac{1}{2} (i\lambda_{ln'n} - \gamma_{ln'n}) = \sum_m C[l]_{mn'} \frac{\partial \langle \psi |}{\partial D[l]_{mn}} \hat{H} |\psi\rangle, \quad (\text{A13})$$

where  $\sum_m C[l]_{mn'}^* C[l]_{mn} = \delta_{n'n}$  and  $\sum_m \dot{C}[l]_{mn'}^* C[l]_{mn} = 0$  are used. Then, multiply again with  $C[l]_{mn}^*$ :

$$i \sum_k \frac{\partial \langle \psi |}{\partial D[l]_{mn}} \frac{\partial |\psi\rangle}{\partial \theta_k} \dot{\theta}_k + \frac{1}{2} \sum_{n'} (i\lambda_{ln'n} - \gamma_{ln'n}) C[l]_{mn'}^* = \hat{P}[l] \frac{\partial \langle \psi |}{\partial D[l]_{mn}} \hat{H} |\psi\rangle. \quad (\text{A14})$$

Using this equation to eliminate  $\lambda$  and  $\gamma$  in Eq. (A12), we get the equation of motion for  $C[l]$ ,

$$i \sum_{n'} \frac{\partial \langle \psi |}{\partial D[l]_{mn}} \frac{\partial |\psi\rangle}{\partial D[l]_{mn'}} \dot{C}[l]_{mn'}^* = (1 - \hat{P}[l]) \frac{\partial \langle \psi |}{\partial D[l]_{mn}} \hat{H} |\psi\rangle, \quad (\text{A15})$$

which can be simplified to

$$i\rho[l] \dot{C}[l]^* = (1 - \hat{P}[l]) \langle \phi | \hat{H}'[l] | \phi \rangle. \quad (\text{A16})$$

The measurement required for time evolution is in the same order as the static VQE algorithm.

In the end, we note that imaginary time evolution might be another approach to finding the ground state, in addition to the iterative method described in the main text. Imaginary time evolution might also be a feasible approach to determine  $C[l]$  as an alternative to solving Eq. (13).

## APPENDIX B: NUMERICAL SIMULATION DETAILS

All numerical quantum circuit simulations are performed using the TENSORCIRCUIT [44] package and the TENCIRCHEM [45] package without considering noise. Classical DMRG simulation is performed using the RENORMALIZER package [46]. We use harmonic oscillator eigenstates for phonon basis states. Using positional states might affect the performance of traditional encodings because of the truncation, however, we expect variational encoding to be insensitive to the choice of phonon basis states at the  $N \rightarrow \infty$  limit. We use Gray code for binary encoding as an improvement to the standard approach [22]. For both ground state simulation and dynamics simulation,  $C[l]$  is initialized as  $C[l]_{mn} = \delta_{mn}$ .

For the VQE simulation of the Holstein model, the circuit parameters  $\vec{\theta}$  are optimized by the L-BFGS-G method implemented in the SCIPY package [47]. The parameter gradient is calculated by autodifferentiation. The initial values for the parameters are set to zero at the first round of the macroiteration. In subsequent macroiterations, the previously optimized parameters are used as the initial value for faster convergence. Equation (13) is solved by the DF-SANE method implemented in SCIPY [47]. Since this is a nonlinear equation, we provide three initial guesses and adopt the one with the lowest energy. The solved  $C[l]$  sometimes does not satisfy the orthonormal condition due to numerical imprecision and the orthonormal condition is enforced by QR decomposition in each macroiteration.

For the VQD simulation of the spin-boson model, the variational Hamiltonian ansatz used is more complex than the VQE simulation. Because  $C[l]$  is complex,  $\hat{B}[l] \hat{h}[l] \hat{B}[l]^\dagger$  spans the whole Hermitian matrix space. Thus, for  $\hat{h}[l]_x$  the whole Pauli matrix set  $\{X, Y, Z, I\}^{\otimes N_i}$  is added to the ansatz. To obtain the quantities required to calculate  $\theta_k$ , the Jacobian of the wave function  $\phi(\vec{\theta})$  is first calculated by autodifferentiation, and then the right-hand side and left-hand side of Eq. (5) in the main text are calculated by matrix multiplication. How to measure the quantities in realistic quantum

circuits is well described in the literature [19]. To calculate  $\hat{C}[l]$ , it is necessary to take the inverse of  $\rho[l]$ , which is sometimes ill-conditioned. We add  $1 \times 10^{-5}$  to the diagonal elements of  $\rho[l]$  for regularization. The time evolution of  $\theta_k$  and  $C[l]$  is carried out using the RK45 method implemented in SCIPY [47]. We observe that the gradient of  $\theta_k$  is usually much larger than  $C[l]$ . Thus, it is possible to evolve the two sets of parameters separately, which deserves further investigation. For Trotterized time evolution,  $N = 16$  and a time step of 0.01 are used.

## APPENDIX C: EXPERIMENTS ON A SUPERCONDUCTING QUANTUM PROCESSOR

### 1. Device parameters

The superconducting quantum processor, as shown in Fig. 3(a) in the main text, is composed of nine computational transmon qubits with each pair of neighboring qubits mediated via a tunable coupler, forming a cross-shaped architecture [42,43]. Each computational qubit has an independent readout cavity for state measurement and  $XY/Z$  control lines for state operation. High-fidelity simultaneous single-shot readout for all qubits is achieved with the help of the multistage amplification with the Josephson parametric amplifier functioning as the first stage of the amplification. The fundamental device parameters including qubit parameters and gate parameters are outlined in Tables II and III, where the parasitic  $ZZ$  interaction between qubits is suppressed by the coupler.

### 2. Experimental details

We use three qubits out of the nine-qubit computer for the two-site Holstein model:

$$\hat{H} = -V(a_1^\dagger a_2 + a_2^\dagger a_1) + \omega b_1^\dagger b_1 + \omega b_2^\dagger b_2 + g\omega a_1^\dagger a_1 (b_1^\dagger + b_1) + g\omega a_2^\dagger a_2 (b_2^\dagger + b_2). \quad (\text{C1})$$



TABLE II. Single qubit gate parameters.  $\omega_r$  is the resonant frequency of the readout cavity for each qubit.  $\omega_{j,\max}$  ( $j = 1 \sim 9$ ) are the maximum resonant frequencies when qubits are biased at the sweet spot.  $\omega_{j,\text{idle}}$  ( $j = 1 \sim 9$ ) are the idle frequencies for implementing the single-qubit operations.  $\alpha_j$  ( $j = 1 \sim 9$ ) are the qubits' anharmonicities.  $T_1$ ,  $T_{2,\text{idle}}$ , and  $T_{2E,\text{idle}}$  are the corresponding energy relaxation time, Ramsey dephasing time, and echoed dephasing time for the qubits measured at the idle frequency. The readout fidelities are typically characterized by detecting each qubit in  $|g\rangle$  ( $|e\rangle$ ) when it is prepared in  $|g\rangle$  ( $|e\rangle$ ), labeled by  $F_{0,j}$  and  $F_{1,j}$ . To mitigate the error coming from the readout infidelity, the outcomes are reconstructed with the calibration matrix through the Bayes' rule. Single-qubit errors  $e_{\text{sq}}$  are measured with randomized benchmarking (RB).

	$Q_0$	$Q_1$	$Q_2$	$Q_3$	$Q_4$	$Q_5$	$Q_6$	$Q_7$	$Q_8$
$\omega_r$ (GHz)	6.874	6.825	6.931	6.901	6.845	6.786	6.991	6.961	6.806
$\omega_{j,\max}$ (GHz)	4.003	4.215	4.479	4.689	4.470	4.479	4.657	4.512	4.362
$\omega_{j,\text{idle}}$ (GHz)	3.988	4.187	4.464	4.668	4.404	4.359	4.641	4.498	4.223
$\alpha_j/2\pi$ (MHz)	-260	-258	-255	-250	-254	-258	-253	-257	-264
$T_1$ ( $\mu\text{s}$ )	35.3	31.6	29.5	27.7	33.9	34.3	33.3	22.1	31.8
$T_{2,\text{idle}}$ ( $\mu\text{s}$ )	11.0	10.2	32.6	38.2	9.1	5.6	43.1	24.1	4.3
$T_{2E,\text{idle}}$ ( $\mu\text{s}$ )	48.2	38.4	47.8	44.2	31.6	21.8	56.8	32.9	18.6
$F_{0,j}$ (%)	96.9	97.4	98.6	98.9	98.7	98.4	96.3	97.2	94.1
$F_{1,j}$ (%)	93.7	94.3	92.5	94.3	94.5	94.6	92.7	92.4	90.9
$e_{\text{sq}}$ (%)	0.07	0.32	0.06	0.07	0.08	0.05	0.06	0.15	0.08

The electronic degree of freedom is mapped to the second qubit. Thus,  $a_1^\dagger a_1$  is mapped to  $\frac{1}{2}(1 + Z_1)$  and  $a_2^\dagger a_2$  is mapped to  $\frac{1}{2}(1 - Z_1)$ . The phonon modes are mapped to the first and the third qubit. With binary encoding and  $N_l = 1$ , the Hamiltonian in the Pauli string form reads

$$\hat{H} = -VX_1 + \frac{1}{2}\omega(1 - Z_0) + \frac{1}{2}\omega(1 - Z_2) + \frac{1}{2}g\omega(1 + Z_1)X_0 + \frac{1}{2}g\omega(1 - Z_1)X_2. \quad (\text{C2})$$

For variational encoding, we assume  $C[l] = C$ . That is, the two modes share the same variational encoder. This is a reasonable assumption for translational invariant systems.  $\hat{b}^\dagger \hat{b} = \sum_m m |m\rangle \langle m|$  is then encoded to

$$\hat{B}(\hat{b}^\dagger \hat{b})\hat{B}^\dagger = \sum_{m'} F_{mm'} |n\rangle \langle n'|, \quad F_{mm'} := \sum_m m C_{mm} C_{mm'}. \quad (\text{C3})$$

It is then possible to express the encoded operator as

$$\hat{B}(\hat{b}^\dagger \hat{b})\hat{B}^\dagger = c_{1i}I + c_{1x}X + c_{1z}Z, \quad (\text{C4})$$

where

$$c_{1i} = (F_{00} + F_{11})/2, \quad c_{1x} = F_{01} = F_{10}, \quad c_{1z} = (F_{00} - F_{11})/2. \quad (\text{C5})$$

Similarly,  $\hat{b}^\dagger + \hat{b}$  is encoded as

$$\hat{B}(\hat{b}^\dagger + \hat{b})\hat{B}^\dagger = c_{2i}I + c_{2x}X + c_{2z}Z \quad (\text{C6})$$

and we omit the explicit expression for  $c_2$  for brevity. The encoded Hamiltonian is then

$$\begin{aligned} \hat{H} = & -VX_1 + \omega(c_{1i}I_0 + c_{1x}X_0 + c_{1z}Z_0) + \omega(c_{1i}I_2 + c_{1x}X_2 + c_{1z}Z_2) \\ & + \frac{1}{2}g\omega(1 + Z_1)(c_{2i}I_0 + c_{2x}X_0 + c_{2z}Z_0) + \frac{1}{2}g\omega(1 - Z_1)(c_{2i}I_2 + c_{2x}X_2 + c_{2z}Z_2). \end{aligned} \quad (\text{C7})$$

TABLE III. Two-qubit gate parameters.  $\omega_{c,\text{idle}}$  are the idle frequencies for each coupler where the ZZ interaction between neighboring computational qubits are maximally suppressed.  $\xi_{ZZ}$  is the residual ZZ interaction between each qubit pair. Two-qubit gates are implemented with the controlled-Z (CZ) and the corresponding gate errors  $e_{\text{iq,CZ}}$  are characterized with RB.

	$Q_0 - Q_1$	$Q_0 - Q_2$	$Q_0 - Q_3$	$Q_0 - Q_4$	$Q_1 - Q_5$	$Q_2 - Q_6$	$Q_3 - Q_7$	$Q_4 - Q_8$
$\omega_{c,\text{idle}}$ (GHz)	5.020	5.445	5.570	5.335	5.325	5.595	5.695	5.355
$ \xi_{ZZ} $ (kHz)	18.0	10.0	5.0	8.0	2.0	3.0	5.0	2.0
$e_{\text{iq,CZ}}$ (%)	1.57	2.22	1.99	2.47	0.91	1.04	1.2	0.96

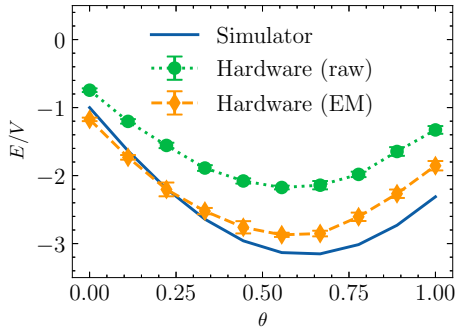
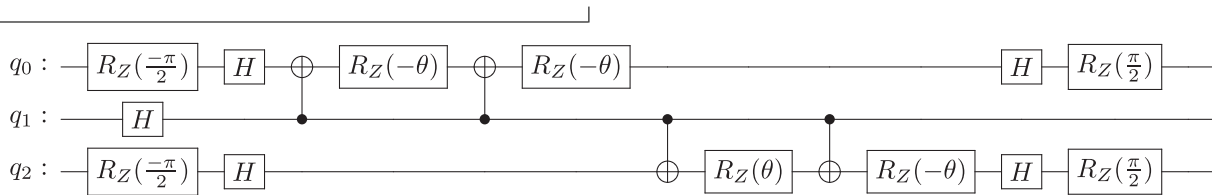


FIG. 4. VQE energy landscape for the two-site Holstein model with binary encoding. For the data from quantum hardware, both raw data and data with readout error mitigation are presented. The error bar indicates the measurement uncertainty.



Each energy term is measured by 8192 shots, and the uncertainty is obtained by repeating the measurement five times and taking the standard deviation. For the update of  $C[l]$ , 4096 shots are performed for each term. Local readout error mitigation is applied for all results presented unless otherwise stated.

In Fig. 4, we plot the energy landscape  $E(\theta)/V$  in VQE with binary encoding. Both raw data and data with local

We use the following ansatz for the parameterized quantum circuit:

$$|\phi\rangle = \prod_{j=1}^2 e^{i\theta_j a_j^\dagger a_j (b_j^\dagger - b_j)} \frac{1}{\sqrt{2}} (|000\rangle + |100\rangle). \quad (C8)$$

Because  $C[1] = C[2]$ , the parameter space can be further simplified by setting  $\theta_1 = \theta_2$ . With binary encoding, the ansatz transforms to

$$|\phi\rangle = e^{i\theta Y_2} e^{-i\theta Z_1 Y_2} e^{i\theta Y_0} e^{i\theta Z_1 Y_0} H_1 |0\rangle. \quad (C9)$$

The ansatz is compiled into the following quantum circuit with four CNOT gates:

readout error mitigation are presented for the energy expectation from quantum hardware. The mitigated landscape is in decent agreement with the perfect simulator. A minimum at around  $\theta = 0.6$  is clearly visible. We note that the perfect simulator is also based on the  $N_l = 1$  ansatz and  $N$  is far smaller than what is physically demanded. Thus, the minimum presented by the perfect simulator cannot be recognized as the ground truth.

[1] J. Bardeen and W. Shockley, Deformation potentials and mobilities in non-polar crystals, *Phys. Rev.* **80**, 72 (1950).  
 [2] M. Cardona and M. L. W. Thewalt, Isotope effects on the optical spectra of semiconductors, *Rev. Mod. Phys.* **77**, 1173 (2005).  
 [3] M. B. Salamon and M. Jaime, The physics of manganites: Structure and transport, *Rev. Mod. Phys.* **73**, 583 (2001).  
 [4] W. E. Pickett, Electronic structure of the high-temperature oxide superconductors, *Rev. Mod. Phys.* **61**, 433 (1989).  
 [5] E. Jeckelmann and S. R. White, Density-matrix renormalization-group study of the polaron problem in the Holstein model, *Phys. Rev. B* **57**, 6376 (1998).  
 [6] E. A. Nowadnick, S. Johnston, B. Moritz, R. T. Scalettar, and T. P. Devereaux, Competition Between Antiferromagnetic and Charge-Density-Wave Order in the Half-Filled Hubbard-Holstein Model, *Phys. Rev. Lett.* **109**, 246404 (2012).  
 [7] A. S. Mishchenko, N. Nagaosa, G. De Filippis, A. de Candia, and V. Cataudella, Mobility of Holstein Polaron at Finite Temperature: An Unbiased Approach, *Phys. Rev. Lett.* **114**, 146401 (2015).  
 [8] X. Cai, Z.-X. Li, and H. Yao, Antiferromagnetism Induced by Bond Su-Schrieffer-Heeger Electron-Phonon Coupling: A Quantum Monte Carlo Study, *Phys. Rev. Lett.* **127**, 247203 (2021).  
 [9] J. Sous, B. Kloss, D. M. Kennes, D. R. Reichman, and A. J. Millis, Phonon-induced disorder in dynamics of optically pumped metals from nonlinear electron-phonon coupling, *Nat. Commun.* **12**, 5803 (2021).  
 [10] W. Li, J. Ren, and Z. Shuai, A general charge transport picture for organic semiconductors with nonlocal electron-phonon couplings, *Nat. Commun.* **12**, 4260 (2021).  
 [11] C. Zhang, J. Sous, D. R. Reichman, M. Berciu, A. J. Millis, N. V. Prokof'ev, and B. V. Svistunov, Bipolaronic High-Temperature Superconductivity, *Phys. Rev. X* **13**, 011010 (2023).  
 [12] S. Lloyd, Universal quantum simulators, *Science* **273**, 1073 (1996).  
 [13] F. Arute, K. Arya, R. Babbush, D. Bacon, J. C. Bardin, R. Barends, R. Biswas, S. Boixo, F. G. Brandao, D. A. Buell *et al.*, Quantum supremacy using a programmable superconducting processor, *Nature (London)* **574**, 505 (2019).  
 [14] S. Xu, Z.-Z. Sun, K. Wang, L. Xiang, Z. Bao, Z. Zhu, F. Shen, Z. Song, P. Zhang, W. Ren *et al.*, Digital simulation of non-Abelian anyons with 68 programmable superconducting qubits, [arXiv:2211.09802](https://arxiv.org/abs/2211.09802).

- [15] J. Preskill, Quantum computing in the NISQ era and beyond, *Quantum* **2**, 79 (2018).
- [16] A. Macridin, P. Spentzouris, J. Amundson, and R. Harnik, Electron-Phonon Systems on a Universal Quantum Computer, *Phys. Rev. Lett.* **121**, 110504 (2018).
- [17] P. J. Ollitrault, G. Mazzola, and I. Tavernelli, Nonadiabatic Molecular Quantum Dynamics with Quantum Computers, *Phys. Rev. Lett.* **125**, 260511 (2020).
- [18] B. Jaderberg, A. Eisfeld, D. Jaksch, and S. Mostame, Recompile-enhanced simulation of electron-phonon dynamics on IBM quantum computers, *New J. Phys.* **24**, 093017 (2022).
- [19] C.-K. Lee, C.-Y. Hsieh, S. Zhang, and L. Shi, Variational quantum simulation of chemical dynamics with quantum computers, *J. Chem. Theory Comput.* **18**, 2105 (2022).
- [20] Y. Wang, J. Ren, W. Li, and Z. Shuai, Hybrid quantum-classical boson sampling algorithm for molecular vibrationally resolved electronic spectroscopy with Duschinsky rotation and anharmonicity, *J. Phys. Chem. Lett.* **13**, 6391 (2022).
- [21] M. M. Denner, A. Miessen, H. Yan, I. Tavernelli, T. Neupert, E. Demler, and Y. Wang, A hybrid quantum-classical method for electron-phonon systems, [arXiv:2302.09824](https://arxiv.org/abs/2302.09824).
- [22] N. P. Sawaya, T. Menke, T. H. Kyaw, S. Johri, A. Aspuru-Guzik, and G. G. Guerreschi, Resource-efficient digital quantum simulation of  $d$ -level systems for photonic, vibrational, and spin- $s$  hamiltonians, *npj Quantum Inf.* **6**, 49 (2020).
- [23] O. Di Matteo, A. McCoy, P. Gysbers, T. Miyagi, R. M. Woloshyn, and P. Navrátil, Improving Hamiltonian encodings with the Gray code, *Phys. Rev. A* **103**, 042405 (2021).
- [24] R. Somma, G. Ortiz, E. Knill, and J. Gubernatis, Quantum simulations of physics problems, *Int. J. Quantum Inform.* **01**, 189 (2003).
- [25] A. Miessen, P. J. Ollitrault, and I. Tavernelli, Quantum algorithms for quantum dynamics: A performance study on the spin-boson model, *Phys. Rev. Res.* **3**, 043212 (2021).
- [26] A. Peruzzo, J. McClean, P. Shadbolt, M.-H. Yung, X.-Q. Zhou, P. J. Love, A. Aspuru-Guzik, and J. L. O'Brien, A variational eigenvalue solver on a photonic quantum processor, *Nat. Commun.* **5**, 4213 (2014).
- [27] J. R. McClean, J. Romero, R. Babbush, and A. Aspuru-Guzik, The theory of variational hybrid quantum-classical algorithms, *New J. Phys.* **18**, 023023 (2016).
- [28] Y. Li and S. C. Benjamin, Efficient Variational Quantum Simulator Incorporating Active Error Minimization, *Phys. Rev. X* **7**, 021050 (2017).
- [29] X. Yuan, S. Endo, Q. Zhao, Y. Li, and S. C. Benjamin, Theory of variational quantum simulation, *Quantum* **3**, 191 (2019).
- [30] D. S. Abrams and S. Lloyd, Quantum Algorithm Providing Exponential Speed Increase for Finding Eigenvalues and Eigenvectors, *Phys. Rev. Lett.* **83**, 5162 (1999).
- [31] A. Aspuru-Guzik, A. D. Dutoi, P. J. Love, and M. Head-Gordon, Simulated quantum computation of molecular energies, *Science* **309**, 1704 (2005).
- [32] I. G. Ryabinkin, R. A. Lang, S. N. Genin, and A. F. Izmaylov, Iterative qubit coupled cluster approach with efficient screening of generators, *J. Chem. Theory Comput.* **16**, 1055 (2020).
- [33] C. Zhang, E. Jeckelmann, and S. R. White, Density Matrix Approach to Local Hilbert Space Reduction, *Phys. Rev. Lett.* **80**, 2661 (1998).
- [34] C. Guo, A. Weichselbaum, J. von Delft, and M. Vojta, Critical and Strong-Coupling Phases in One-and Two-Bath Spin-Boson Models, *Phys. Rev. Lett.* **108**, 160401 (2012).
- [35] X. Yuan, J. Sun, J. Liu, Q. Zhao, and Y. Zhou, Quantum Simulation with Hybrid Tensor Networks, *Phys. Rev. Lett.* **127**, 040501 (2021).
- [36] J. Eisert, M. Cramer, and M. B. Plenio, Colloquium: Area laws for the entanglement entropy, *Rev. Mod. Phys.* **82**, 277 (2010).
- [37] T. Holstein, Studies of polaron motion: Part I. The molecular-crystal model, *Ann. Phys.* **8**, 325 (1959).
- [38] T. Holstein, Studies of polaron motion: Part II. The "small" polaron, *Ann. Phys.* **8**, 343 (1959).
- [39] A. J. Leggett, S. Chakravarty, A. T. Dorsey, M. P. Fisher, A. Garg, and W. Zwerger, Dynamics of the dissipative two-state system, *Rev. Mod. Phys.* **59**, 1 (1987).
- [40] D. Wecker, M. B. Hastings, and M. Troyer, Progress towards practical quantum variational algorithms, *Phys. Rev. A* **92**, 042303 (2015).
- [41] H. Wang and M. Thoss, From coherent motion to localization: II. Dynamics of the spin-boson model with sub-Ohmic spectral density at zero temperature, *Chem. Phys.* **370**, 78 (2010).
- [42] F. Yan, P. Krantz, Y. Sung, M. Kjaergaard, D. L. Campbell, T. P. Orlando, S. Gustavsson, and W. D. Oliver, Tunable Coupling Scheme for Implementing High-Fidelity Two-Qubit Gates, *Phys. Rev. Appl.* **10**, 054062 (2018).
- [43] X. Li, T. Cai, H. Yan, Z. Wang, X. Pan, Y. Ma, W. Cai, J. Han, Z. Hua, X. Han *et al.*, Tunable Coupler for Realizing a Controlled-Phase Gate with Dynamically Decoupled Regime in a Superconducting Circuit, *Phys. Rev. Appl.* **14**, 024070 (2020).
- [44] S.-X. Zhang, J. Allcock, Z.-Q. Wan, S. Liu, J. Sun, H. Yu, X.-H. Yang, J. Qiu, Z. Ye, Y.-Q. Chen, C.-K. Lee, Y.-C. Zheng, S.-K. Jian, H. Yao, C.-Y. Hsieh, and S. Zhang, Tensorcircuit: A quantum software framework for the NISQ era, *Quantum* **7**, 912 (2023).
- [45] W. Li, J. Allcock, L. Cheng, S.-X. Zhang, Y.-Q. Chen, J. P. Mailoa, Z. Shuai, and S. Zhang, Tencirchem: An efficient quantum computational chemistry package for the NISQ era, [arXiv:2303.10825](https://arxiv.org/abs/2303.10825).
- [46] J. Ren, W. Li, T. Jiang, Y. Wang, and Z. Shuai, The RENORMALIZER package, <https://github.com/shuaigroup/renormalizer> (2021).
- [47] P. Virtanen, R. Gommers, T. E. Oliphant, M. Haberland, T. Reddy, D. Cournapeau, E. Burovski, P. Peterson, W. Weckesser, J. Bright, S. J. van der Walt, M. Brett, J. Wilson, K. J. Millman, N. Mayorov, A. R. J. Nelson, E. Jones, R. Kern, E. Larson, C. J. Carey, Í. Polat, Y. Feng, E. W. Moore, J. VanderPlas, D. Laxalde, J. Perktold, R. Cimrman, I. Henriksen, E. A. Quintero, C. R. Harris, A. M. Archibald, A. H. Ribeiro, F. Pedregosa, P. van Mulbregt, and SciPy 1.0 Contributors, SciPy 1.0: Fundamental algorithms for scientific computing in Python, *Nat. Methods* **17**, 261 (2020).